Synthesis and Characterization of Mixed ZnSe/GaP Semiconductor Species Included in the Sodalite Structure

Kelly L. Moran,† Thurman E. Gier,† William T. A. Harrison,†,‡ Galen D. Stucky,*,† Hellmut Eckert,*,† Klaus Eichele,§ and Roderick E. Wasylishen*,§

Contribution from the Departments of Chemistry, University of California, Santa Barbara, California 93106, and Dalhousie University, Halifax, Nova Scotia, Canada B3H 4J3

Received June 14, 1993®

Abstract: The synthesis of the solid solution series $Ga_xZn_{(8-x)}P_xSe_{(2-x)}[BO_2]_{12}$ ($x = 0, 0.5, 1, 2$) is reported and the local and average long-range structures are discussed based on X-ray diffraction data, UV/visible spectroscopic measurements, and a variety of field-dependent static and magic angle spinning solid state NMR experiments. Inclusion of GaP within the borate sodalite analogue results in the formation of an isolated $^{31}P,^{69,71}Ga$ spin pair that exhibits resolved scalar coupling in the ^{31}P MAS NMR spectra. The analysis reveals that there are four different intracage structures distributed in small domains throughout the powdered materials and these are identified as $[Zn_4Se]^{6+}$, $[GaZn_3P]^{6+}$, $[Zn_4P]^{5+}$ and, by inference, $[Ga_2Zn_2P]^{7+}$. ^{31}P spin diffusion experiments suggest that the materials are single phase solid solutions, and powder X-ray diffraction data, which do not reveal more than one phase for any composition, support this conclusion.

Introduction

The optoelectronic properties of compounds can be dramatically altered by inclusion into the sodalite framework, which is one of several reasons why this zeolite structure type remains the focus of ongoing research efforts in many laboratories.[1] First described by Pauling in 1930,[2] the sodalite structure consists of a three-dimensional array of face-sharing cuboctahedral "cages" supported by intracage tetrahedra, a schematic of which is shown in Figure 1. The general composition of the cubic sodalite unit cell is $M_8X_2[TO_2]_{12}$, in which tetrahedral atoms, T, linked by bridging oxygen atoms[3] form the anionic framework that encloses charge-balancing M_4X tetrahedra. Both naturally-occurring and synthetic isotypes are known for a myriad of compositions[4] (M = Li, Na, K, Ag, Ca, Sr, Zn, Cd, ...; X = Br, Cl, OH, P, As, O, S, Se, Te, SO_4, WO_4, ...; T = Be, B, Al, Ga, Si, Ge, ...).

Sodalite oxide frameworks typically have high dielectric constants[5] and act as electrostatic barriers between adjacent cages, an isolation effect that perturbs the electronic structure of the intracage species. Inclusion of potassium halide into aluminosilicate sodalite, for example, results in enhanced cathodochromic sensitivity, and these materials are used in display devices. This enhancement due to inclusion has been attributed to framework-assisted isolation of individual F centers, electrons trapped at halogen vacancies, as well as greater separation of the electrons from the hole centers with which they recombine.[6]

The framework electrostatic isolation effect is observed readily by MAS NMR spectroscopy of the cage center anions. The single ^{77}Se MAS NMR resonance of the sodalite analogue zinc selenide borate, $Zn_8Se_2[BO_2]_{12}$, is shifted far upfield relative to bulk ZnSe,[7] which suggests greater localization of electron density at the cage center; that is, the delocalization of the bulk semiconductor is blocked by the framework electric field and by the extended cage-to-cage distance. Cage size and separation distance can be controlled by substitution of the framework atoms with consequent changes in the optoelectronic properties, as demonstrated in the genthelvites, sodalite analogues of composition $Zn_8X_2[BeSi_yGe_{(1-y)}O_4]_6$ (X = S, Se, Te).[8]

Another method for fine-tuning the optoelectronic properties of sodalites is to vary the intracage composition. For example, deposition of sodium vapor onto the optically transparent sodalite $Na_6[AlSiO_4]_6$[9] results in the buildup of $Na_4^{4+}[e^-]$ clusters inside the cages, in which the electron, e^-, is not tightly bound to the cluster.[10] By controlling the amount of sodium that enters the

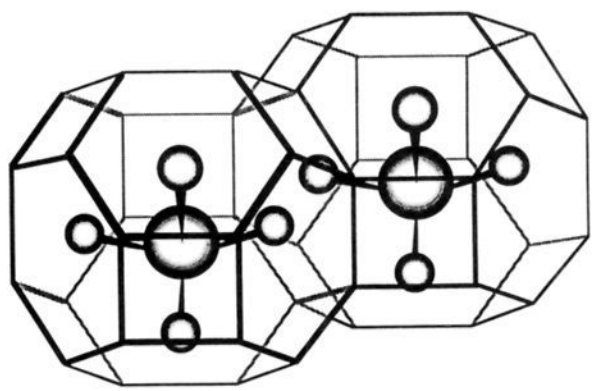

Figure 1. A schematic diagram of the sodalite structure with composition $M_8X_2[TO_2]_{12}$. The T atoms are represented by vertices of the cuboctahedral cages and are connected *via* bridging oxygens which are not shown. The central anion X is represented by the large circle at the centers of the cages, surrounded by four M cations in a tetrahedral arrangement; the cations are directed toward alternating 6-ring faces.

† University of California.

‡ Present address: Department of Chemistry, University of Houston, Houston, TX 77204.

§ Dalhousie University.

® Abstract published in *Advance ACS Abstracts,* October 15, 1993.

(1) See, for example: Stucky, G. D.; Srdanov, V. I.; Harrison, W. T. A.; Gier, T. E.; Keder, N. L.; Moran, K. L.; Haug, K.; Metiu, H. I. In *Supramolecular Architecture: Synthetic Control in Thin Films and Solids*; Bein, T., Ed.; American Chemical Society: Washington, DC, 1992; pp 294–313. Ozin, G. A.; Kuperman, A.; Stein, A. *Angew. Chem., Int. Ed. Engl.* **1989**, *28*, 359–376.

(2) Pauling, L. *Z. Krist.* **1930**, *74*, 213–225.

(3) The synthesis of a nonoxide-framework sodalite analogue has been reported: Schnick, W.; Lücke, J. *Angew. Chem., Int. Ed. Engl.* **1992**, *31*, 213–215.

(4) Taylor, D. *Contrib. Mineral. Petrol.* **1967**, *16*, 172–188.

(5) Van Doorn, C. Z.; Schipper, D. J.; Bolwijn, P. T. *J. Electrochem. Soc.* **1972**, *119*, 85.

(6) Faughnan, B. W.; Heyman, P. M.; Gorog, I.; Shidlovsky, I. *Advances in Image Pickup and Display*; Academic Press, Inc.: New York, 1981; Vol. 4, pp 87–155.

(7) Moran, K. L.; Ott, A. W.; Gier, T. E.; Harrison, W. T. A.; Eckert, H.; Stucky, G. D. *Mater. Res. Soc. Symp. Proc.* **1992**, *242*, 249–254.

(8) Moran, K. L.; Kamber, I.; Gier, T. E.; Harrison, W. T. A.; Ott, A. W.; Eckert, H.; Stucky, G. D. Manuscript in preparation.

(9) $Na_6[AlSiO_4]_6$ is the dehydroxylated and dehydrated form of $Na_8[AlSiO_4]_6(OH)_2 \cdot 2H_2O$. See, for example: Engelhardt, G.; Felsche, J.; Sieger, P. *J. Am. Chem. Soc.* **1992**, *114*, 1173–1182.

(10) Haug, K.; Srdanov, V. I.; Stucky, G. D.; Metiu, H. *J. Chem. Phys.* **1992**, *96*, 3495.

0002-7863/93/1515-10553$04.00/0

cages, materials which range in color from pale blue to black can be synthesized.[11]

As part of ongoing investigations of the correlations between structure, composition, and optoelectronic properties in sodalite materials, we report the synthesis and characterization of the solid solution series $Ga_xZn_{(8-x)}P_xSe_{(2-x)}[BO_2]_{12}$. The borate sodalite framework has a net charge of –6 which is compensated by a $[Zn_4Se]^{6+}$ tetrahedron inside each cage. Substitution of isovalent GaP for ZnSe is possible due to the size similarities of the atoms; the covalent radii of Ga, Zn, P, and Se are 1.26, 1.25, 1.06, and 1.16 Å, respectively. We describe the average long-range structure of these materials based on results of powder X-ray diffraction and UV/visible spectroscopic measurements. Local electronic effects and compositional variations are characterized by MAS NMR spectroscopy, a technique well-known for elucidation of short range order in amorphous, disordered, and compositionally complex materials.[12] Specifically, we report here a structural description of these materials based on the ^{77}Se MAS NMR spectra of the cage center anions and a detailed analysis of the ^{31}P MAS and static NMR spectra of the GaP-substituted species measured at different magnetic field strengths.

Experimental Section

Materials. Boric acid and zinc oxide as well as electronic grade ZnSe and GaP were used as purchased from Fisher Scientific and Strem Chemicals, Inc., respectively.

Synthesis. A starting material of nominal stoichiometry ZnB_2O_4 was prepared from ZnO and boric acid heated in air at 550 °C for several hours; powder XRD showed this to be a mixture of ZnB_4O_7 and ZnO. This material was ground well with a stoichiometric amount of the III–V or II–VI compound, loaded into a graphitized quartz ampule,[13] heated gently under vacuum with a torch to remove physisorbed water, and flame-sealed. The sealed ampule was heated in a furnace at 900–950 °C for 12–36 h.

The products, recovered as powders, generally contain excess bulk semiconductor. All of the bulk GaP and most of the ZnSe were removed by stirring the powders for 48 h in an aqueous solution of Br_2 adjusted to a pH of 6 with hypochlorite solution (bleach). Previously we reported[7] the optical spectrum of $Zn_8Se_2[BO_2]_{12}$, which we had mistakenly believed was free of bulk ZnSe; subsequent experiments have revealed that the absorption at 475 nm, erroneously attributed to the sodalite, is due to residual bulk ZnSe in the sample.

Characterization. Structure Determinations: The crystal structures of the solution end members, $Zn_6Ga_2P_2[BO_2]_{12}$ and $Zn_8Se_2[BO_2]_{12}$, were determined by Rietveld refinements against powder X-ray diffraction data. High-resolution data were collected for flat-plate samples of the various materials over 12-h periods on a Scintag PAD-X automated diffractometer operating in a θ–θ geometry of 2θ between 20 and 100°, with a typical step size of 0.02° (Cu Kα radiation, λ = 1.541 78 Å). The resulting patterns could be indexed with body-centered cubic unit cells, with dimensions of $a \approx 7.61$–7.68 Å, depending on the sodalite cage contents. The starting atomic model for each refinement was taken from that of $Zn_8O_2[BO_2]_{12}$,[14] which crystallizes in space group $I\bar{4}3m$.

The Rietveld refinements (program GSAS[15]) progressed smoothly and profile (scale factor, zero-point error, unit cell parameter, background coefficients, peak shape descriptors) and atomic positional and thermal parameters were progressively added to the model as variables in the normal way. For each refinement a 5-parameter pseudo-Voigt function was used to describe the X-ray line shape and its width variation with scattering angle, and the background was modeled by a 3-term Fourier cosine series function.

In the $I\bar{4}3m$ atomic model, there are four distinct sites: one tetrahedral framework boron atom, one "framework" oxygen atom, one tetrahedral (three oxygen atom neighbors + one extra-framework anion) guest cation (M), and one tetrahedral (four guest-cation neighbors) guest anion site (X). Boron occupies the (1/4, 1/2, 0) special positions (crystallographic site symmetry 4..), oxygen (x, x, z) with $x \approx 0.15$ and $z \approx 0.43$ (symmetry ..m), M (x, x, x) with $x \approx 0.17$ (symmetry .3m), and X (0, 0, 0) (symmetry $43m$). In $Zn_6(GaP)_2[BO_2]_{12}$, where both Zn and Ga occupy the same atomic site, the relative proportions of each element were fixed according to the starting compositions of the reaction and refined with appropriate positional and thermal constraints. Refining this model type resulted in a satisfactory convergence to the final unit cell parameters listed in Table I, with R_p, R_{wp} residuals of 4.26, 6.95% and 3.86, 6.30% for the GaP and ZnSe end members, respectively.

Table I. Unit Cell Length (a) and Selected Distances for the Series $Zn_6(GaP)_x(ZnSe)_{2-x}[BO_2]_{12}$ and Bulk Semiconductors[a]

compd	a (Å)	M–X distance (Å)	X–X distance[b] (Å)
$x = 0$	7.6801(4)	2.366(2)	6.6511(4)
$x = 0.5$	7.672(2)		6.644(2)
$x = 1$	7.656(2)		6.630(2)
$x = 2$	7.6139(9)	2.207(2)	6.5938(9)
ZnSe		2.453(1)	4.004(1)
GaP		2.3596(1)	3.8528(1)

[a] Calculated from ref 17. [b] In the sodalite compounds, this is the distance between cage centers through the 6-rings, solely determined by the unit cell constants.

Elemental analysis, performed at Galbraith Laboratories, Knoxville, TN, on a sample with starting stoichiometry $x = 1$, shows a Ga:P ratio of 1.01, close to the expected value of unity. UV/visible spectra were obtained in reflectance mode by means of a $BaSO_4$ integrating sphere on a Cary-14 monochromator upgraded with a computer interface by On-Line Instrument Systems, Inc., Bogart, GA. Spectra were corrected against a $BaSO_4$ background.

All of the NMR experiments were performed on a General Electric GN-300 spectrometer with 7.0 and 4.7 T magnets, using high speed MAS probes manufactured by Doty Scientific, Inc., Columbia, SC. ^{77}Se MAS NMR data were collected at a spectral frequency of 57.3 MHz (7.0 T) using a pulse width of 8.5 μs (90° flip angle) and recycle delay of at least 30 min; chemical shifts are referenced to CdSe. Measurement of the ^{71}Ga MAS NMR signal was attempted at both 7.0 and 4.7 T field strengths (93 and 61 MHz, respectively) with a 2-μs pulse width and 1-s delay. ^{31}P MAS NMR spectra were measured at frequencies of 121.6 (7.0 T) and 81.0 (4.7 T) MHz. A pulse width of 2.25 μs (approximately 30° flip angle) was used with a recycle delay of 10 min and spectra are referenced to H_3PO_4. Static ^{31}P spin–echo measurements were made at 7.0 T with a $\pi/2$–t_1–π pulse sequence; the 90° pulse width was set to 6.25 μs. ^{31}P MAS spectral spin diffusion experiments were performed at 4.7 T with a rotor-synchronized DANTE pulse sequence $(\theta$–$t_1^{-1})_\pi$–τ–$\pi/2$ (SPARTAN).[16] One signal was set on resonance at approximately 81 MHz and selectively inverted by a total of ten short pulses of width 1.25 μs separated by 150 μs. Four scans were acquired at a total of seven different τ delays, ranging from 50 ms to 900 s, with a recycle delay of 15 min.

Results and Discussion

All of the compounds in the $Ga_xZn_{(8-x)}P_xSe_{(2-x)}[BO_2]_{12}$ series crystallize in the body-centered cubic space group $I\bar{4}3m$, characteristic of sodalites with one type of framework tetrahedral atom.[18] The topological details of the $M_8X_2(TO_2)_{12}$ sodalite structure are fully described elsewhere.[19] Unit cell parameters and selected distances are listed in Table I. The geometrical parameters of the various framework (B,O) and guest (M,X) species are typical and are available as supplementary material.

The results of the UV/vis spectroscopic measurements, shown in Figure 2, describe the average electronic structure of these inclusion materials. The absorption bands of the GaP-containing solutions indicate the existence of a well-defined electronic transition in the sodalite compounds. For the ZnSe-based end member ($x = 0$) the absorption edge is presumably deep in the UV region and beyond the measurement capabilities of our

(11) Srdanov, V. I.; Haug, K.; Metiu, H.; Stucky, G. D. *J. Phys. Chem.* **1992**, *96*, 9039–9043.
(12) Eckert, H. *Prog. NMR Spectrosc.* **1992**, *24*, 159–293.
(13) To prevent reaction of borate starting materials with the quartz, ampules were coated with a thin graphite film: the inside walls of the ampule are wetted with acetone and strongly heated with a torch until completely coated.
(14) Smith-Verdier, P.; Garcia-Blanco, S. *Z. Krist.* **1980**, *151*, 175.
(15) Larson, A. C.; Von Dreele, R. B. *GSAS Users Guide, Los Alamos Report*. 1988, LAUR 86-748.
(16) Moran, L. B.; Berkowitz, J. K.; Yesinowski, J. P. *Phys. Rev. B* **1992**, *45*, 5347.
(17) Donnay, J. D. H., Ed.; *Crystal Data: Determinative Tables*, 3rd ed.; JCPDS-International Centre for Diffraction Data: Swarthmore, PA, 1928; Vol. 4.
(18) Depmeier, W. *Z. Krist.* **1992**, *199*, 75–89.
(19) Hassan, I.; Grundy, H. D. *Acta Crystallogr.* **1984**, *B40*, 6–13.

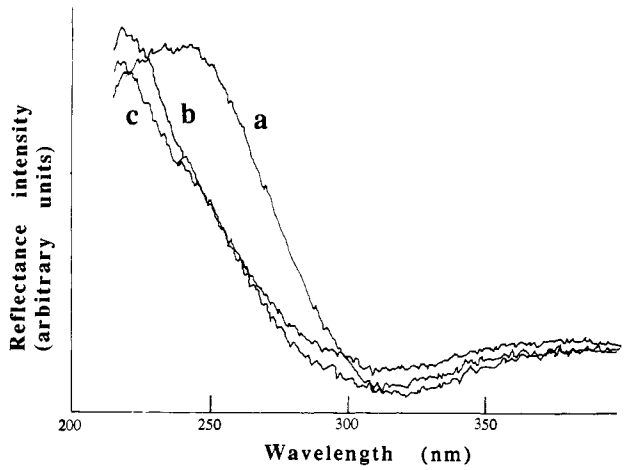

Figure 2. UV/vis reflectance spectra for the solid solutions $Ga_xZn_{(8-x)}P_xSe_{(2-x)}[BO_2]_{12}$: (a) $x = 2$; (b) $x = 1$; (c) $x = 0.5$.

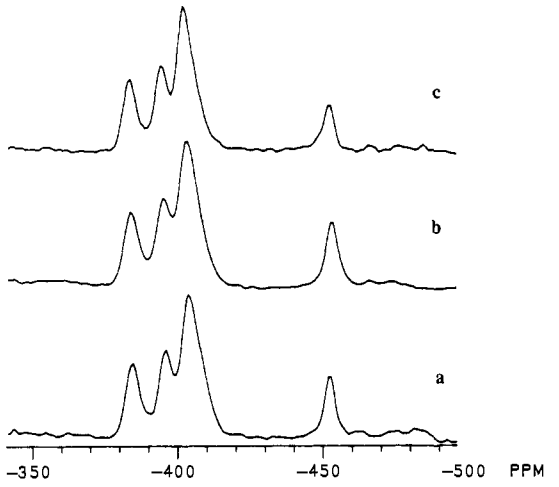

Figure 3. ^{31}P MAS NMR spectra for the series $Ga_xZn_{(8-x)}P_xSe_{(2-x)}[BO_2]_{12}$ measured at a magnetic field strength of 4.7 T: (a) $x = 2$; (b) $x = 1$; (c) $x = 0.5$.

instrumentation. The spectrum of the end member $Zn_6Ga_2P_2[BO_2]_{12}$ is blue-shifted relative to bulk GaP (554 nm) and exemplifies the electronic isolation effect as a result of inclusion. The two solid solutions ($x = 0.5$ and 1) exhibit identical electronic transition energies, within experimental error, that are blue-shifted relative to the GaP end member. This observation suggests that in the GaP end member, for example, there may exist weak cage-to-cage electronic coupling that is interrupted as ZnSe is introduced into the framework. None of the samples exhibited room temperature photoluminescence; the nonradiative relaxation suggests strong coupling to lattice phonons.

Further support for the electrostatic isolation effect of the framework is provided by MAS NMR of the central anions in the series. Within experimental error, the ^{77}Se MAS spectra are invariant to substitution with GaP in the structure. Each solid solution ($x = 0, 0.5, 1$) has a single ^{77}Se resonance at approximately −332 ppm relative to CdSe. The fact that the shift does not change as GaP is added to the structure indicates that the cage center is electronically isolated from neighboring cages. Following the usual chemical shift arguments, the upfield chemical shift relative to that of bulk ZnSe, at +124 ppm, reflects a diminished paramagnetic contribution, suggesting a greater localization of electron density at the cage center Se^{2-} anion, compared to that at the anionic sites in the ZnSe zincblende lattice.

Analogous to the ^{77}Se MAS results, the ^{31}P MAS NMR spectra are invariant to substitution in the series $Ga_xZn_{(8-x)}P_xSe_{(2-x)}[BO_2]_{12}$, as shown in Figure 3, and the resonances are shifted upfield relative to that of bulk GaP (−143 ppm relative to H_3PO_4). Unlike the ^{77}Se MAS NMR spectra, however, the ^{31}P MAS NMR spectra consist of two groups of peaks: a multiplet

Table II. Chemical Shifts (in ppm vs H_3PO_4) and Peak Separations (in Hz) of the ^{31}P Resonances in $Ga_xZn_{(8-x)}P_xSe_{(2-x)}[BO_2]_{12}$

compd	A	B	C	D	A–B	B–C	A–C
			$B_0 = 7.0$ T				
$x = 2$	−390.0	−396.9	−402.0	−453.6	838	697	1535
$x = 1$	−389.4	−396.3	−401.5	−453.1	843	628	1471
$x = 0.5$	−388.8	−395.1	−400.3	−453.0	809	628	1437
			$B_0 = 4.7$ T				
$x = 2$	−384.8	−396.2	−403.9	−453.0	922	628	1550
$x = 1$	−384.3	−395.3	−403.9	−453.0	889	698	1587
$x = 0.5$	−383.9	−394.5	−402.2	−452.1	858	628	1486

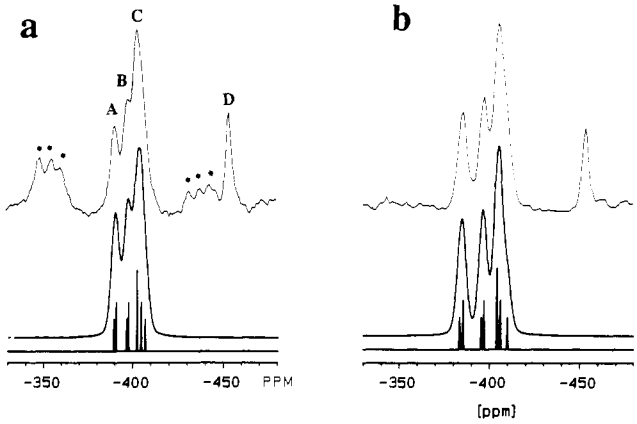

Figure 4. Field-dependent ^{31}P MAS spectra of $Ga_2Zn_6P_2[BO_2]_{12}$: (a) 7.0 T and (b) 4.7 T. Spinning sidebands are labeled with asterisks and chemical shifts of signals A, B, C, and D are listed in Table II. Top traces are experimental spectra and bottom traces are computer simulated spectra, using the parameters described in the text.

of three peaks with the intensity ratio 1:1:2, the center of gravity of which is positioned at −398 ppm, and a single peak at −453 ppm. The ^{31}P MAS spectra of $Ga_2Zn_6P_2[BO_2]_{12}$ at two magnetic field strengths, 4.7 and 7.0 T, are shown in Figure 4 and the chemical shifts and peak separations within the multiplet A–C and the single peak D are listed in Table II.

As revealed by Figure 4 and Table II, the peak positions of A–C on a ppm scale are field dependent and hence suggest the influence of $^{69,71}Ga,^{31}P$ spin–spin coupling. Since ^{69}Ga (natural abundance 60.4%) and ^{71}Ga (39.6%) both have a nuclear spin of $^3/_2$, one might anticipate the high-resolution ^{31}P MAS NMR spectrum of a molecule containing the $^{69,71}Ga,^{31}P$ spin pairs to consist of two sets of four equally-spaced peaks, each associated with one of the allowed components of $^{69,71}Ga$ nuclear spin along the magnetic field, m_s. However, the asymmetric and field-dependent separations within the multiplet at −398 ppm (Figure 4) indicate a strong perturbation of the $^{69,71}Ga$ Zeeman levels by the quadrupolar interaction. One consequence of the breakdown of the so-called high-field approximation is that dipolar interactions involving quadrupolar nuclei are not completely eliminated by magic angle spinning.[20] As a result, high-resolution MAS

(20) (a) Kundla, E.; Alla, M. *Proceedings of the Congress Ampere*, 20th, *Tallinn, 1978*; Kundla, E. I., Lippmaa, E. T., Saluvere, T., Eds.; Springer-Verlag: Berlin, 1979; p 92. (b) Lippmaa, E.; Alla, M.; Raude, H.; Telaar, R.; Heinmaa, I.; Kundla, E. *Proceedings of the XXth Congress Ampere, 20th Tallinn, 1978*; Kundla, E. I., Lippmaa, E. T., Saluvere, T., Eds.; Springer-Verlag: Berlin, 1978; p 87. (c) Mariq, M. M.; Waugh, J. S. *J. Chem. Phys.* **1979**, *70*, 3300. (d) Opella, S. J.; Frey, M. H.; Cross, T. A. *J. Am. Chem. Soc.* **1979**, *101*, 5856. (e) Groombridge, C. J.; Harris, R. K.; Packer, K. J.; Say, B. J.; Tanner, S. F. *J. Chem. Soc., Chem. Commun.* **1980**, 174. (f) Frey, M. H.; Opella, S. J. *J. Chem. Soc., Chem. Commun.* **1980**, 474. (g) Fleming, W. W.; Fyfe, C. A.; Lyerla, J. R.; Vanni, H.; Yannoni, C. S. *Macromolecules* **1980**, *13*, 460. (h) Diesveld, J. W.; Menger, E. M.; Edzes, H. T.; Veeman, W. S. *J. Am. Chem. Soc.* **1980**, *102*, 7935. (i) Opella, S. J.; Hexem, J. G.; Frey, M. H.; Cross, T. A. *Phil. Trans. R. Soc. London* **1981**, *299A*, 665. (j) Naito, A.; Ganapathy, S.; McDowell, C. A. *J. Chem. Phys.* **1981**, *74*, 5393. (k) Zumbulyadis, N.; Henrichs, P. M.; Young, R. H. *J. Chem. Phys.* **1981**, *75*, 1603. (l) Hexem, J. G.; Frey, M. H.; Opella, S. J. *J. Chem. Phys.* **1982**, *77*, 3847. (m) Böhm, J.; Fenzke, D.; Pfeifer, H. *J. Magn. Reson.* **1983**, *55*, 197. (n) Harris, R. K.; Olivieri, A. C. *Progr. NMR Spectrosc.* **1992**, *24*, 435–456.

NMR spectra of spin-$^1/_2$ nuclei that are J coupled to quadrupolar nuclei are not generally symmetrical. Instead, the separations between the peaks are "squeezed" at one end and "stretched" at the other.[21-27]

In cases where the quadrupolar coupling constant, χ, is smaller than the Zeeman interaction, such quadrupolar perturbed multiplets in the MAS NMR spectra of spin-$^1/_2$ nuclei have been successfully analyzed by application of first-order perturbation theory.[28] To first order, the ^{31}P MAS NMR transitions of phosphorus nuclei, indirectly and directly spin–spin coupled to a quadrupolar nucleus S, are given by:[28]

$$\nu_m = -m|J| - \frac{S(S+1) - 3m^2}{S(2S-1)}d \qquad (1)$$

where J is the ^{69,71}Ga,^{31}P indirect spin–spin coupling constant, $S = {}^3/_2$ for ^{69,71}Ga, $m = {}^3/_2, {}^1/_2, -{}^1/_2$, and $-{}^3/_2$, and the residual dipolar coupling d is given by:

$$d = \frac{-3\chi(D - \Delta J/3)}{20\nu_s}[3\cos^2\beta^D - 1 + \eta\sin^2\beta^D\cos 2\alpha^D] \qquad (2)$$

D is the Ga,P direct dipolar coupling constant, $(\mu_o/4\pi)\gamma_{Ga}\gamma_P r_{Ga,P}^{-3}(\hbar/2\pi)$, where $r_{Ga,P}^{-3}$ is the inverse cube of the Ga,P internuclear separation, ΔJ is the anisotropy in the indirect spin–spin coupling tensor, ν_s is the ^{69}Ga or ^{71}Ga Larmor frequency (48.14 and 61.16 MHz at $\mathbf{B}_0$ = 4.7 T), χ is the ^{69}Ga or ^{71}Ga nuclear quadrupolar coupling constant, $e^2q_{zz}Q/h$, and η is a parameter which describes the asymmetry of the electric field gradient (EFG) tensor at the Ga nucleus, $(eq_{xx} - eq_{yy})/eq_{zz}$, with $|eq_{zz}| \geq |eq_{yy}| \geq |eq_{xx}|$. The azimuthal and polar angles α^D and β^D define the orientation of the dipolar vector in the principal axis system of the EFG tensor. In eq 2 we have assumed that the unique component of the J tensor is parallel to the dipolar vector. To first order, the appearance of the spectrum is independent of the sign of J.[20n]

From the two ^{31}P MAS NMR spectra obtained at different magnetic field strengths, the multiplet centered at δ_{iso} = –398 ppm can be analyzed unambiguously to yield values of the indirect spin–spin coupling constants, J, and the residual dipolar coupling, d. In order to obtain the calculated spectra shown in Figure 4, both isotopes ^{69}Ga and ^{71}Ga were included into the calculation with J and d scaled according to the magnetogyric ratios, $\gamma(^{69}\text{Ga})/\gamma(^{71}\text{Ga}) = 0.787$, and nuclear quadrupole moments, $Q(^{69}\text{Ga})/Q(^{71}\text{Ga}) = 1.59$, respectively.[29,30] Although the presence of the minor component ^{71}Ga,^{31}P does not result in additional peaks within the multiplets shown in Figure 4, it causes shoulders most apparent in the low-frequency region of the ^{31}P MAS NMR spectrum obtained at 81 MHz. The parameters used to generate the calculated spectra shown in Figure 4 are the following: $J(^{69}\text{Ga},^{31}\text{P})$ = 560 Hz, $J(^{71}\text{Ga},^{31}\text{P})$ = 712 Hz, and $d(^{69}\text{Ga})$ = +192 Hz, $d(^{71}\text{Ga})$ = +121 Hz at 4.7 T and $d(^{69}\text{Ga})$ = +128 Hz, $d(^{71}\text{Ga})$ = +81 Hz at 7.0 T. A mixed Gaussian–Lorentzian line broadening function consisting of 75% Gaussian line shape and line widths of 400 (4.7 T) and 600 Hz (7.0 T) was employed. Since the ratio of the line widths observed at the two different magnetic field strengths equals the ratio of the field strengths $\mathbf{B}_0$, a chemical shift dispersion appears to be the source of the broadening.

The observation of spin–spin coupling of phosphorus to one gallium nucleus is attributed to a $[GaZn_3P]^{6+}$ cage, in which gallium is tetrahedrally coordinated to one phosphorus atom and three oxygen atoms. Based on this 3-fold local symmetry at the site of the gallium nucleus, the ^{69,71}Ga,^{31}P dipolar vector is assumed to be collinear (β^D = 0) with the z axis of the axially symmetric EFG tensor (η = 0). Assuming crystallographic site equivalence of the Ga and Zn atoms in the structure, the calculated Ga–P separation is 2.207 Å, from which the dipolar coupling constants for the spin pairs ^{69}Ga,^{31}P (1060 Hz) and ^{71}Ga,^{31}P (1350 Hz) can be calculated. Furthermore, if $\Delta J/3$ is assumed to be negligible, it is possible to use eq 2 to estimate the quadrupolar coupling constants for the gallium nuclei to be –29 (^{69}Ga) and –18 MHz (^{71}Ga). While these are only crude estimates, it is clear that the Ga quadrupolar coupling constants are of the same order of magnitude as the Larmor frequencies at 4.7 T. Consequently, the large second-order quadrupolar interaction deduced here for gallium is expected to lead to ^{71}Ga line broadening in excess of 200 kHz, and this probably explains our inability to detect a ^{71}Ga NMR signal. In order to assess the validity of the first-order perturbation approach used here, we have examined an analogous spin-$^1/_2$, spin-$^3/_2$ system, which Menger and Veeman[21] previously treated "exactly". Comparison of the results of exact calculations[21] with those of the first-order approach indicates that the latter calculations are valid provided that $K < 0.2$, where $K = \chi/4\nu_s$ for $S = {}^3/_2$. In the spin system studied here, $K < 0.2$ for ^{69}Ga and ^{71}Ga at both applied magnetic fields; thus the analysis is valid and supported by the fact that the observed ^{69}Ga and ^{71}Ga splittings in the ^{31}P MAS NMR spectra at both fields are reproduced by the first-order calculations.

The peak at –453 ppm in the ^{31}P MAS NMR spectrum must be attributed to a different type of phosphorus species not bonded to gallium. The question remains as to the nature of the nearest neighbor environment of the phosphorus nucleus. The relative spin counts of the ^{31}P resonances indicate that this singlet moiety accounts for 12–14% of the total phosphorus in each sample; if this represents a separate crystallographic phase it would be detected by high-resolution XRD measurements, unless, of course, the symmetry and the lattice parameters are equivalent to the solution containing the Ga-coupled phosphorus.

To address the question of possible phase separation in these samples, ^{31}P MAS spectral spin diffusion measurements were carried out between the dominant signal near –403 ppm and the peak at –453 ppm. As previously shown, spectral spin diffusion is a sensitive probe of the dipole–dipole interactions between two spins which are close enough spatially to exchange Zeeman polarization. Such exchange is possible even for inequivalent sites under MAS conditions if there is level crossing between dipole-coupled spins during the MAS rotor period.[16,31] The rate of spin diffusion decreases as the spatial separation increases, proportional to the inverse sixth power of the internuclear distance.[32] Thus we would expect no net polarization transfer in our materials if they were phase separated.

The results of the SPARTAN experiment for the $Ga_2Zn_6P_2[BO_2]_{12}$ sample are shown in Figure 5. The strongest resonance at –403 ppm has been selectively inverted with the DANTE sequence and the system is allowed to relax for a time τ before application of a nonselective $\pi/2$ pulse prior to the FID acquisition. Measurements are made at varying τ and the resulting spectra are a map of the time-dependent polarization transfer between spins at different frequencies. The detailed τ-dependence of the normalized resonance intensity for the –453-ppm peak is given in the figure caption. The apparent initial slight increase at very short τ values is most likely due to imperfections in the DANTE sequence. The subsequent decrease over the time interval 2 s $\leq \tau \leq$ 60 s is evidence of spin diffusion. At longer τ values, the peak

(21) Menger, E. M.; Veeman, W. S. *J. Magn. Reson.* **1982**, *46*, 257.
(22) Harris, R. K. *J. Magn. Reson.* **1988**, *78*, 389.
(23) Olivieri, A. *J. Am. Chem. Soc.* **1992**, *114*, 5758.
(24) Chu, P.-J.; Lunsford, J. H.; Zalewski, D. J. *J. Magn. Reson.* **1990**, *87*, 68.
(25) Lindner, E.; Fawzi, R.; Mayer, H. A.; Eichele, K.; Pohmer, K. *Inorg. Chem.* **1991**, *30*, 1102.
(26) Gobetto, R.; Harris, R. K.; Apperley, D. C. *J. Magn. Reson.* **1992**, *96*, 119.
(27) Eichele, K.; Wasylishen, R. E.; Corrigan, J. F.; Doherty, S.; Sun, Y.; Carty, A. J. *Inorg. Chem.* **1993**, *32*, 121.
(28) Olivieri, A. C. *J. Magn. Reson.* **1989**, *81*, 201.
(29) Mason, J., Ed. *Multinuclear NMR*; Plenum Press: New York, 1987.
(30) Popkova, L. A.; Guryanova, E. N.; Volkov, A. F. *J. Mol. Struct.* **1982**, *83*, 341.
(31) Zhang, Z.; Kennedy, J. H.; Eckert, H. *J. Am. Chem. Soc.* **1992**, *114*, 5775.
(32) Kubo, A.; McDowell, C. A. *J. Chem. Soc., Faraday Trans. 1* **1988**, *84*, 3713–3730. Suter, D.; Ernst, R. R. *Phys. Rev. B* **1985**, *32*, 5608–5627.

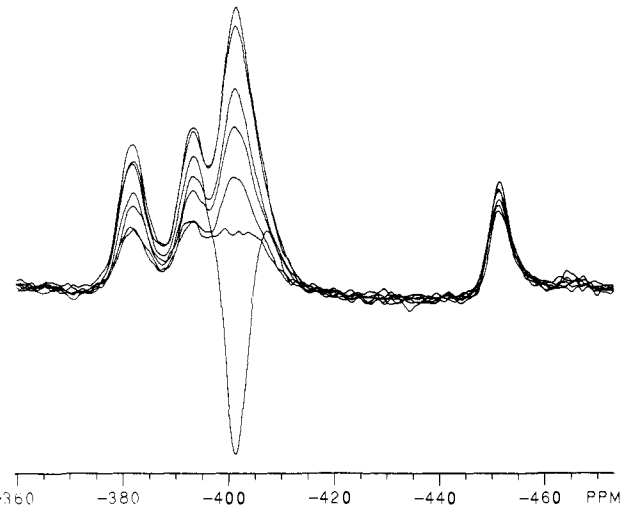

Figure 5. Results of the ^{31}P spin diffusion experiment for the $Ga_2Zn_6P_2[BO_2]_{12}$ sample, carried out at 4.7 T as described in the text. Upon selective inversion of the peak at –403 ppm, the intensity of the signal at –453 ppm changes in the following manner [τ, $I(\tau)/I(50\text{ ms})$]: 50 ms, 1.00; 2 s, 1.10; 8 s, 1.04; 32 s, 0.87; 60 s, 0.76; 240 s, 0.89; 900 s, 0.94;

intensities increase again due to the effects of spin–lattice relaxation. While magnetization transfer is most efficient within the *J*-coupled multiplet, as expected, the decrease observed in the intensity of the singlet at –453 ppm clearly indicates spatial proximity between the two types of phosphorus atoms. Likewise, selective inversion of the ^{31}P resonance at –453 ppm shows cross-relaxation effects involving the *J*-coupled multiplet. The distance between P nuclei in adjacent cages in this sample is 6.594 Å, which is of appreciable magnitude and explains the overall weakness of the effect. Based on these results and the XRD observations, it is reasonable to assume that the material is single phase and that the two types of phosphorus reside in adjacent cages.

Based on the absence of observable *J*-coupling to $^{69,71}Ga$ isotopes we assign the signal at –453 ppm to a phosphorus coordinated to four zinc atoms, forming the tetrahedron $[Zn_4P]^{5+}$. This assignment is further supported by the absence of discernible spinning sidebands in the 7.0 T spectrum (see Figure 4) indicating a small chemical shift anisotropy as expected for a very symmetric environment. Stoichiometrically there is one Ga for every P nucleus in the material, as confirmed by elemental analysis, which must be accounted for in the model we describe. Based on stoichiometric and charge restrictions, the $[Zn_4P]^{5+}$ cage center is most likely adjacent to a cage containing $[Ga_2Zn_2P]^{7+}$ and the populations of these species must be equal. While we do not observe a corresponding ^{31}P signal for the $[Ga_2Zn_2P]^{7+}$ species, we expect the signal intensity of this species to be spread out considerably more than for $[GaZn_3P]^{6+}$ due to the stronger $^{69,71}Ga,^{31}P$ dipole coupling, the increased *J*-coupling multiplicity, and the lower symmetry at the phosphorus site. Possibly the ^{31}P signal for this species is either broadened beyond detection or obscured by the spectrum attributed to the $[GaZn_3P]^{6+}$ species. Unfortunately we cannot distinguish clearly between these two possibilities by absolute spin quantitation, because of the low expected relative intensity of the "missing" signal (12–14%). Also there are no known model compounds containing Zn and Ga in the nearest neighbor environment of a tetrahedrally coordinated P atom, therefore it is not possible to provide more definitive evidence of this assignment.

While charge restrictions require proximity of the $[Zn_4P]^{5+}$ and $[Ga_2Zn_2P]^{7+}$ cages, the overall distribution of the four intracage species throughout the structure remains to be addressed. The lack of any significant trend of ^{31}P and ^{77}Se chemical shifts with composition argues in favor of P-rich and Se-rich microdomains. More precise information about this distribution is obtained by measuring the homonuclear dipole–dipole couplings between the phosphorus cage centers. The internuclear distances r_{ij} between like nuclei in a solid are related to the second moment, M_{2d}, of the NMR spectral resonance line by the following equations, derived from van Vleck theory:[33]

$$M_{2d} = {}^3/_5(\mu_o/4\pi)^2 I(I+1)\gamma^4\hbar^2 N^{-1}\sum_{i\neq j} r_{ij}^{-6} \quad (3a)$$

or

$$M_{2d} = {}^4/_{15}(\mu_o/4\pi)^2 I(I+1)\gamma^4\hbar^2 N^{-1}\sum_{i\neq j} r_{ij}^{-6} \quad (3b)$$

where γ is the magnetogyric ratio, I is the spin quantum number, and N is the number of nuclei for which M_{2d} is calculated. Equation 3a is used if the interacting nuclei have identical resonance frequencies. On the other hand, if the interacting nuclei have resonance frequency differences that are large compared to the dipolar coupling constant, eq 3b must be used. The latter is often the case if inhomogeneous broadening, site distribution effects, or heteronuclear dipolar couplings create magnetic inequivalences. As discussed above, there are strong static heteronuclear $^{69,71}Ga,^{31}P$ interactions in these materials; we would expect that the measured values of M_{2d} would approximate those given by eq 3b.

Experimentally, the second moment is measured by the pulse sequence $\pi/2$–t_1–π. The static spin–echo technique serves to refocus all interactions linear in I_z resulting in the formation of an echo of the signal at time $2t_1$.[34] The homonuclear spin–spin interactions are not refocussed in this experiment and thus cause a decay in the intensity of the spin–echo with increasing evolution time $2t_1$. Assuming multiple spin interactions, the decay is approximated as Gaussian and is given by:

$$I(2t_1)/I(0) = \exp\{-M_{2d}(2t_1)^2/2\} \quad (4)$$

where $I(0)$ is the extrapolated intensity of the echo at the time origin. Previous studies of model compounds have shown that this analysis yields the correct M_{2d} values as predicted from eq 3b.[35]

The spin–echo decay and the fit to eq 4 for the solid solution $x = 1$ are shown in Figure 6, from which it is clear that the Gaussian approximation is valid for these materials. Figure 7 compares the measured and calculated second moments for all of the samples studied. The curves a and c, from eqs 3a and 3b, respectively, are calculated assuming *all* cage centers are occupied by phosphorus; thus only the cage-to-cage distance, based on unit cell size, affects the magnitude of M_{2d}. These curves describe the results expected if the samples formed P- and Se-rich microdomains. On the other hand, the dashed lines b and d correspond to M_{2d} calculated for a completely random distribution of P- and Se-filled cages in the samples, based on eqs 3a and 3b, respectively, and account for the increasing P–P distances (on average) as ZnSe is added to the structure. All of the calculated curves include homonuclear dipolar interactions from the first, second, and third nearest cage center spheres, with a total radius of about 20 Å.

The measured second moments of the solid solutions most closely resemble curve c, which indicates that there is much stronger homonuclear dipolar coupling than would be expected based on a random distribution of phosphorus in the solid solutions. These data are evidence of phosphorus-rich domains in the solid solutions. The existence of measurable domains in other sodalite analogues has been demonstrated by various high-resolution TEM studies.[36]

(33) Van Vleck, J. H. *Phys. Rev.* **1948**, *74*, 1168.
(34) Lathrop, D.; Eckert, H. *J. Am. Chem. Soc.* **1989**, *111*, 3536–3541.
(35) Franke, D. R.; Maxwell, R. S.; Lathrop, D.; Eckert, H. *J. Am. Chem. Soc.* **1991**, *113*, 4822. Lathrop, D.; Franke, D. R.; Maxwell, R. S.; Tepe, T.; Flesher, R.; Zhang, Z.; Eckert, H. *Solid State Nucl. Magn. Reson.* **1992**, *1*, 73–83.
(36) (a) Hassan, I.; Grundy, H. D. *Can. Mineral.* **1989**, *27*, 165. (b) Tsuchiya, N.; Takeuchi, Y. *Z. Krist.* **1985**, *173*, 273.

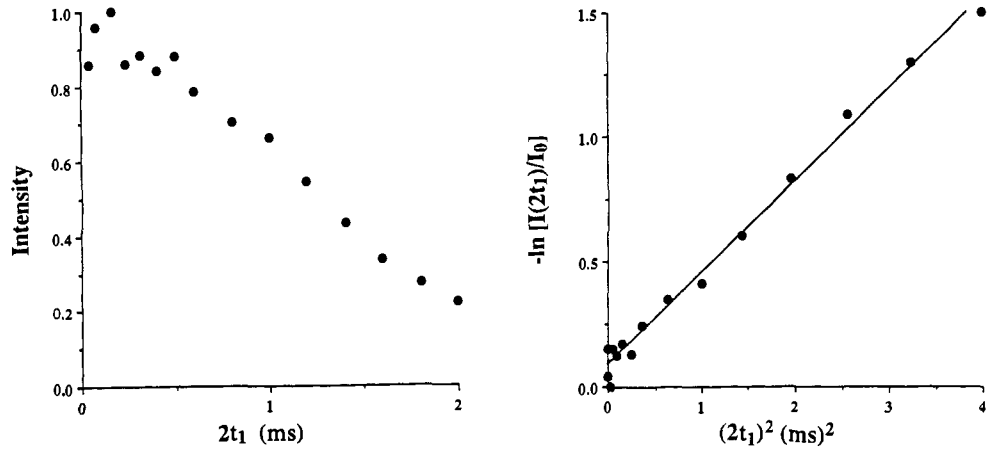

Figure 6. Results of the ^{31}P static spin–echo experiment for the solid solution $GaZn_7PSe[BO_2]_{12}$. (Left) Normalized decay in the spin–echo intensity as a function of $2t_1$; (right) fit of experimental data to eq 2.

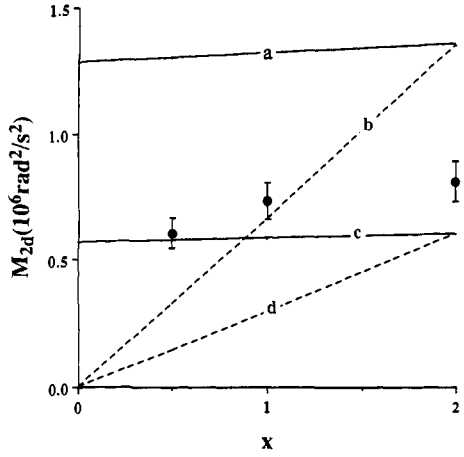

Figure 7. Experimental and calculated compositional dependence of ^{31}P second moments for the solution series $Ga_xZn_{(8-x)}P_xSe_{(2-x)}[BO_2]_{12}$: (a) eq 3a, assuming phosphorus at all cage centers (cluster model); (b) eq 3a, assuming a random distribution of phosphorus atoms over the cage centers; (c) eq 3b, assuming phosphorus at all cage centers (cluster model); (d) eq 3b, assuming a random distribution of phosphorus atoms in the sample.

The calculated curves in Figure 7 do not account for the preferred coupling of $[Zn_4P]^{5+}$ and $[Ga_2Zn_2P]^{7+}$ cages, expected on the basis of local charge considerations. It is reasonable to assume that these cages would be joined at the 6-ring faces of the cuboctahedra, which represent the smallest distance between the contents of adjacent cages. Preferential contact through the 6-ring faces would result in stronger ^{31}P–^{31}P homonuclear dipolar coupling and hence a larger M_{2d} than that calculated for curve c. Because the samples exhibit strong heteronuclear dipolar coupling, which discounts the use of eq 3a (curves a and b) for these solutions, we believe that the discernible discrepancy between the observed and calculated M_{2d} may be attributable to these preferential cage contacts.

Conclusion

Inclusion of ZnSe and GaP in the borate sodalite framework results in intriguing local and average long-range optoelectronic properties. The materials are single phase solid solutions that exhibit interesting optical absorption features. The absorption edge of ZnSe borate is apparently blue-shifted, relative to bulk ZnSe, to the far-UV region and that of the GaP-included end member is blue-shifted significantly from bulk GaP. The average optoelectronic properties of the two solutions are identical and the common absorption edge appears at an energy somewhere between those of the two end members. These results suggest that there is a cooperative electronic effect between like cages in the pure end members that is blocked in the solutions as the contents vary from cage to cage.

MAS NMR results suggest that the sodalite structure serves to isolate, electronically and magnetically, the species within the cages. In the GaP-included sodalite, the ^{31}P NMR spectra of an isolated $^{69,71}Ga$,^{31}P spin pair have been observed and analyzed. The indirect coupling J(Ga,P) has been determined and discussed. Four different intracage structures have been identified in these single-phase materials as $[Zn_4Se]^{6+}$, $[GaZn_3P]^{6+}$, $[Zn_4P]^{5+}$ and, by inference, $[Ga_2Zn_2P]^{7+}$. Measurement of the homonuclear ^{31}P–^{31}P dipolar coupling strength indicates that the phosphorus-containing cages are not distributed randomly throughout the sodalite structure; rather they group together in microdomains. These domains, however, are too small to be detected by lab source X-ray diffraction.

Identification of the various intracage compositions cannot be confirmed by X-ray diffraction due to the similarity in electron density between the zinc and gallium atoms; with neutron diffraction data it may be possible to observe the small domains and to confirm the existence of the individual moieties due to the loss of local intracage (3-fold) symmetry in the $[Ga_2Zn_2P]^{7+}$ species, for example.[37] Overall, the results of this study illustrate the power of combined selective ^{31}P NMR approaches to elucidate the local electronic structures and atomic arrangements present in these nanocomposites.

Acknowledgment. Funding was provided by the following: the NSF Science and Technology Center for Quantized Electronic Structures, Grant No. DMR 91-20007; National Science Foundation DMR89-13738 (H.E.); and by the Office of Naval Research (G.D.S.). R.E.W. acknowledges the financial support of NSERC of Canada. We also thank the Shell Development Company for donation of a Bruker CXP-200 NMR spectrometer.

Supplementary Material Available: Tables of atomic coordinates, fractional occupancies, and isotropic thermal parameters for $Zn_6(GaP)_2[BO_2]_{12}$ and $Zn_8Se_2[BO_2]_{12}$, Figure 1 showing the final observed, calculated, and difference profile plots for the Rietveld refinement of $Zn_6(GaP)_2[BO_2]_{12}$, and a diagram of the crystal structure of the solid solution series $Ga_xZn_{8-x}P_xSe_{2-x}[BO_2]_{12}$ (3 pages). Ordering information is given on any current masthead page.

(37) Private communication with Michael A. Estermann of E.T.H., Zurich, Switzerland.